

# Strong Coupling in Two-Phase Metamaterials Fabricated by Sequential Self-Assembly

Jelena Wohllwend,\* Georg Haberfehlner, and Henning Galinski

Self-assembly processes provide the means to achieve scalable and versatile metamaterials by “bottom-up” fabrication. Despite their enormous potential, especially as a platform for energy materials, self-assembled metamaterials are often limited to single phase systems, and complex multi-phase metamaterials have scarcely been explored. A new approach based on sequential self-assembly (SSA) that enables the formation of a two-phase metamaterial (TPM) composed of a disordered network metamaterial with embedded nanoparticles (NPs) is proposed. Taking advantage of both the high-spatial and high-energy resolution of electron energy loss spectroscopy (EELS), inhomogeneous localization of light in the network is observed, concurrent with dipolar and higher-order localized surface plasmon modes in the nanoparticles. Moreover, it is demonstrated that the coupling strength deviates from the interaction of two classical dipoles when entering the strong coupling regime. The observed energy exchange between two phases in this complex metamaterial, realized solely through self-assembly, implies the possibility to exploit these disordered systems for plasmon-enhanced catalysis.

## 1. Introduction

Plasmonic metamaterials and metasurfaces have attracted tremendous research interest in the field of photocatalysis and artificial photosynthesis because high absorption and local field enhancement in these plasmonic systems offer the potential to efficiently drive chemical processes by sunlight.<sup>[1–6]</sup>

To this effect, the damping of plasmons by non-radiative decay into so-called “hot” carriers, that is, electron-hole (e-h) pairs,

has sparked considerable and long lasting theoretical and experimental interest. Especially, antenna-reactors complexes, often made of nanoparticle dimers, utilize hot carriers generated in the plasmon-enhanced near field to enhance chemical reactions by light.<sup>[7,8]</sup> For example, in ultra-small gaps “hot” carriers can be used to drive polymerization reactions.<sup>[9,10]</sup>

However, to guarantee technological impact these concepts must find a scalable analog.

Among the strategies to design large scale nanostructured materials, self-assembly is a fundamental design principle ubiquitous in living organism.<sup>[11]</sup> Intriguingly, architectures created by self-assembly can be attributed to a single physical principle, the minimization of free energy in a nonuniform system. This principle is very general and applies to all length scales and material classes.<sup>[12]</sup>

In fact, self-assembly has shown to be an effective approach to design large scale plasmonic metasurfaces<sup>[13]</sup> for structural color displays using thin-film growth mechanisms,<sup>[14]</sup> to assemble plasmonic metamaterials by exploiting fluid instabilities<sup>[15]</sup> and to create fractal metamaterials for sensing applications based on self-assembly of hot aerosols.<sup>[16]</sup> Despite the richness self-assembly offers for materials design, its full-potential including sequential combination of different self-assembly processes remains to be exploited.

Here, we propose sequential self-assembly (SSA) as an adaptable and versatile platform to fabricate two-phase metamaterials (TPMs), that is, metamaterials with at least two functional components. We select phase separation<sup>[17–19]</sup> in an immiscible system and self-assembly by chemical dealloying<sup>[20,21]</sup> to realize our two-phase metamaterial (**Figure 1a**). While the assembly by phase separation is due to the spontaneous formation of domains from an unstable mixture,<sup>[22]</sup> self-organization in chemical dealloying results from a reaction-diffusion process, where the less noble metal in a solid solution is dissolved at the liquid-solid interface.<sup>[23]</sup>

## 2. Results and Discussion

Magnetron sputtering is ideally suited to generate conditions that facilitate phase separation on the nanoscale during growth.<sup>[18,24]</sup> Especially in immiscible co-sputtered systems, the interplay between the kinetics, such as the mobility difference of different

J. Wohllwend, H. Galinski  
Laboratory for Nanometallurgy  
Department of Materials  
ETH Zurich, Zürich 8093, Switzerland  
E-mail: jelena.wohllwend@mat.ethz.ch

G. Haberfehlner  
Institut für Elektronenmikroskopie und Nanoanalytik  
TU Graz  
Graz 8010, Austria

The ORCID identification number(s) for the author(s) of this article can be found under <https://doi.org/10.1002/adom.202300568>

© 2023 The Authors. Advanced Optical Materials published by Wiley-VCH GmbH. This is an open access article under the terms of the Creative Commons Attribution-NonCommercial License, which permits use, distribution and reproduction in any medium, provided the original work is properly cited and is not used for commercial purposes.

DOI: 10.1002/adom.202300568

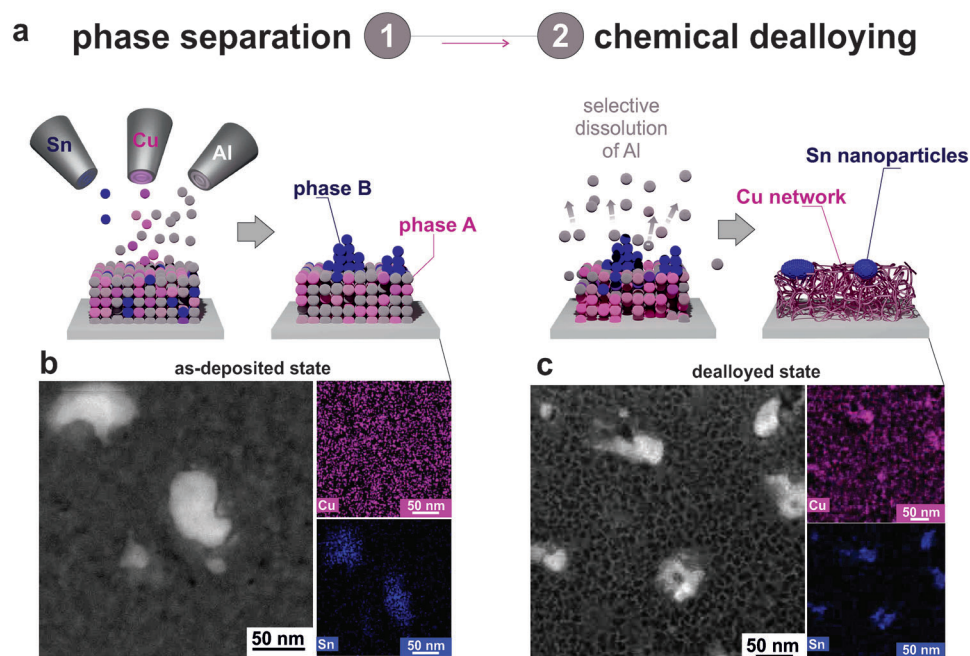


**Figure 1.** Sequential self-assembly of disordered two-phase metamaterials. a) Schematic illustration of sequential self-assembly. First phase separation, meaning the Al-Cu-Sn thin films separate into phase A (Al + Cu) and phase B (Sn nanoparticles) during the co-sputter process of Al, Cu, and Sn. Second chemical dealloying, where the ternary material self-organizes into a Cu-based network and Sn nanoparticles by selective dissolution of Al. b) High-angle annular dark field (HAADF) micrographs and elemental distribution maps of the as-deposited state confirming the phase separation of Al-Cu-Sn into a two-phase metamaterial, with phase A being the Cu-Al thin film and phase B being Sn NPs, during deposition. c) HAADF micrographs and elemental distribution maps of the dealloyed state showing a Cu based disordered network with randomly distributed Sn NPs.

elements, and the local thermodynamic potential favor phase separation. In case of binary Cu-Mo thin films the phase separation can be controlled by the substrate temperature, resulting in self-assembly of either vertically-, laterally-, or randomly- organized phases.<sup>[25]</sup> We transplant this approach to the ternary Al-Cu-Sn system which in the bulk phase diagram features a prominent miscibility gap (see also Supporting Information).<sup>[26]</sup> Specifically, the deposition conditions were adjusted to favor growth kinetics that result in the formation of two phases at the nanoscale, visible in Figure 1b.

After the initial phase separation, we make use of a second self-assembly process: chemical dealloying. Dealloying is the selective removal of the less noble alloy component to form an open-porous disordered network by a linearly propagating diffusion front.<sup>[21]</sup> Here, the majority element Al is removed in the dealloying process. The resulting self-organized two-phase system, consisting of a Cu network with embedded Sn nanoparticles (NPs), is shown in Figure 1c.

Elemental distribution maps of Cu and Sn in Figure 1b,c indicate the formation of two phases, that is, Sn NPs and a Al-Cu thin film respectively a Cu network, through the SSA process (see also Supporting Information).

To study the formation of these two-phase systems and to map their local plasmonic environment, we use electron energy loss spectroscopy (EELS). EELS has emerged as the ideal technique to characterize hybrid metamaterials on the nanoscale.<sup>[27–30]</sup> EELS is able to excite and spatially probe surface and bulk plasmons. Thereby, chemical information can be obtained from the bulk

plasmon peak of plasmonic nanostructures as the energy of the bulk plasmon is directly proportional to the electron density.

We study the local evolution of the bulk plasmon mode by EELS (Figure 2), to confirm the formation of a two phase-system. To underline the robustness and reproducibility of our SSA approach, two different samples are shown. The bulk plasmon energy  $E_{\text{bulk}} = \hbar \sqrt{\frac{n_e e^2}{\epsilon_0 m_e}}$  scales with the free electron density  $n_e$ , and therefore is well suited to identify local chemical variations including phase formation at the nanoscale (Figure 2). To this extent, two different phases can be identified in the EELS maps and spectra shown in Figure 2: the Cu-based nanometric network with  $\omega_p = 21.7$  eV and Sn NPs with their bulk plasmon peak centered at  $\omega_p = 14.0$  eV. The measured bulk plasmon energy of Sn is in good agreement with values reported in literature,<sup>[31,32]</sup> whereas the Cu peak slightly deviates from reported values.<sup>[32,33]</sup> This deviation might stem from residual Al or partial oxidation shifting the bulk plasmon peak to higher energies. Remarkably, both size and shape of the NP phase can be engineered by changing the kinetics of phase separation during growth (see also Supporting Information), so that NPs with spherical (Figure 2a), ellipsoidal (Figure 3a) and arbitrary shapes (Figure 1b,c) can be realized. Thus, self-organization during growth provides a mechanism to tune the plasmonic resonance of these particles, which critically depends on the prevailing geometry.<sup>[29]</sup> Generally, modification of the NP geometry not only affects the resonance frequency, but also enables to alter the absorption cross-section<sup>[34]</sup> and near-field enhancement.<sup>[35]</sup>

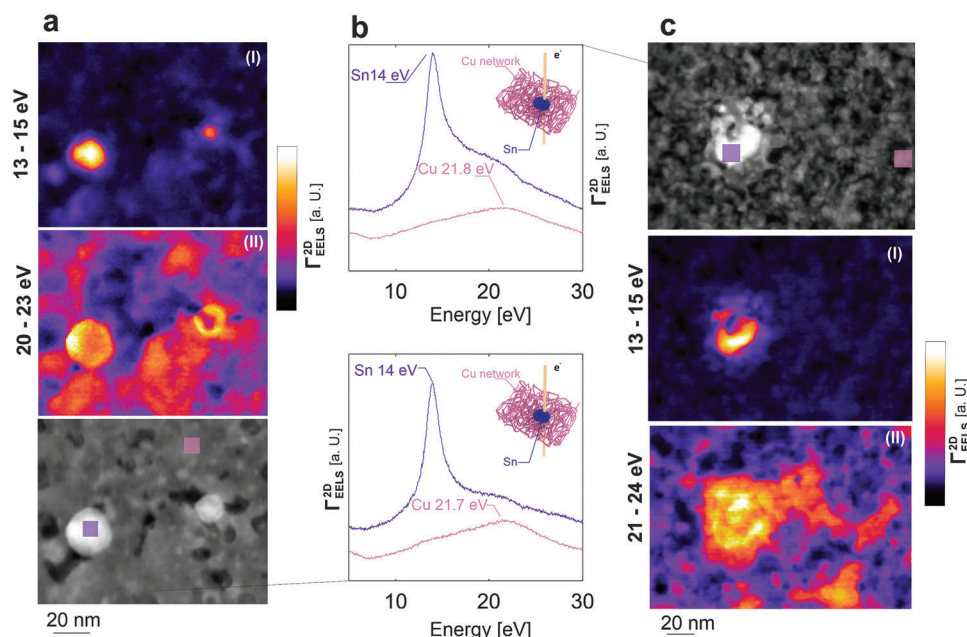


**Figure 2.** Chemical analysis by mapping bulk plasmon modes a,c) EELS analysis of two metamaterials including HAADF micrographs of Cu-Sn networks with embedded Sn NPs, color-coded maps of bulk plasmon excitation of Sn NPs (I) and Cu-Sn network (II). b) The specific regions of the spectra are indicated with colored squares in the HAADF micrographs. A clear shift of  $\Delta E = 8$  eV between the two bulk plasmon peaks is observed, confirming the formation of a two-phase system.

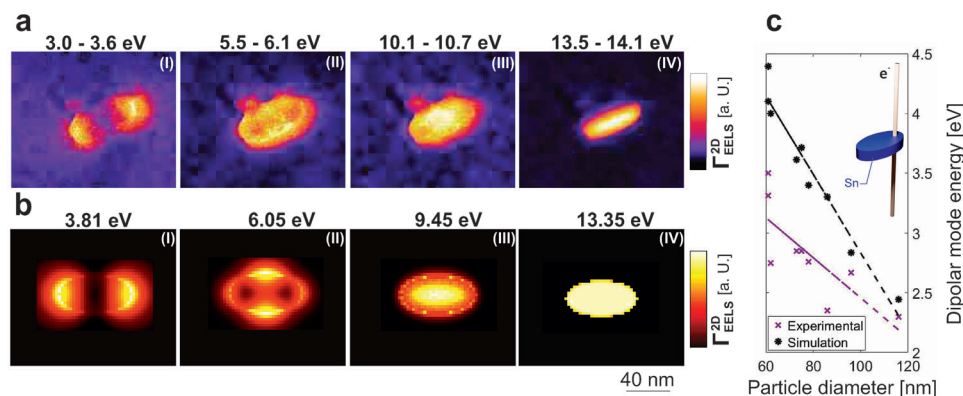


**Figure 3.** Localized Surface Plasmon Resonances (LSPR) in Sn nanoparticles a,b) measured and simulated EELS maps for selected energies corresponding to the intensity maxima identified in the EELS spectra with (I) dipolar mode, (II) quadrupolar mode, (III) breathing mode, and (IV) bulk plasmon mode. c) Simulated and measured dependence of the dipolar mode energy on the long semi-axis of the Sn nanoparticle.

We begin to study the complex photonic environment of the two-phase network metamaterial, by characterizing the modal properties of the NP phase. The sustained localized surface plasmon (LSP) modes of a selected ellipsoidal Sn NP excited by the electron beam are reported in Figure 3. To achieve further insight on the characteristics of this modes, the EELS signal is mapped within a selected energy range centered around the resonance energy of each mode (Figure 3a I–IV). The Sn NP exhibits several localized SP resonances including a dipolar mode centered at 3.3 eV and higher order (HO) modes including a quadrupolar mode (5.8 eV) and a breathing mode<sup>[36]</sup> (10.4 eV). Quadrupolar modes and breathing modes are typically optically dark excitations, meaning they cannot be excited by light, highlighting again the advantages of characterizing plasmonic structures by

EELS.<sup>[36]</sup> The bulk plasmon peak in Figure 3a IV visualizes the spatial dimensions of the Sn NP and additionally confirms the chemical nature of this particle.<sup>[31]</sup>

Figure 3b compares the experimentally obtained EELS data with electron energy-loss simulations performed using the MNPBEM toolbox.<sup>[37]</sup> Here, the Sn NP is modeled as an elliptical cylinder to match the shape of the experimentally observed NP, with a height of 15 nm using refractive index data from literature.<sup>[38]</sup> Complementary simulations for spherical particles can be found in Supporting Information. Impressively, the obtained resonance energy and simulated EELS maps shown in Figure 3b are in good agreement with the experiment. While all experimentally observed modes are reproduced, slight deviations in the resonance energies are found. These deviations can



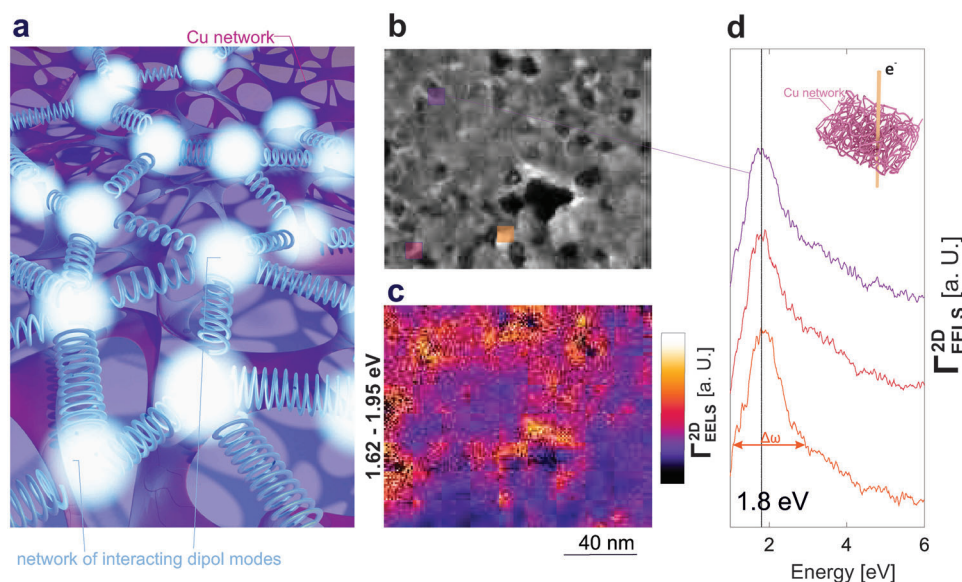


**Figure 4.** Global network mode in disordered network metamaterials. a) Schematic illustration of the plasmonic response in a network metamaterial, exhibiting a set of coupled electromagnetic dipole-like resonances (balls and springs), whose distribution and interaction is given by the local connectivity and curvature of the dealloyed Cu-network. b) HAADF image of a disordered Cu network metamaterial. c) Color coded EELS map containing global network modes (GNMs) with an energy of 1.8 eV forming local hot spots on network studs and d) EELS spectra from different hot spot regions,  $10 \times 10 \text{ nm}^2$ , highlighting the efficient localization of light over a broad frequency range ( $\Delta\omega = 1.8 \pm 0.076 \text{ eV}$ ). The specific regions are indicated with colored squares in (b).

be explained by the influence of the surrounding Cu-network on the non-retarded resonance energy of the modes<sup>[39]</sup> as well as by deviations of the experimental NPs from the simulated elliptical cylinder.

The LSP modes of metallic NPs are highly dependent on shape and size, a trend also observed in our Sn NPs.<sup>[29,40]</sup> With an increase in particle diameter (long semi-axis) the dipolar mode is red shifted, as shown in Figure 3c, where the dipolar mode energy is displayed as a function of the particle diameter. A similar linear scaling is found for simulated elliptical Sn NPs (Figure 3c), while the difference in slope might originate again from the surrounding medium as well as from size and shape differences between the simulated elliptical cylinders and the experimentally measured imperfect Sn NPs.<sup>[41]</sup>

Next, we characterize the plasmonic response of the second phase: the Cu-based dealloyed network. These networks can be represented as coupled dipole-like networks (Figure 4a), where the disordered network traps and localizes surface plasmon (SP) waves.<sup>[42]</sup> Figure 4b shows a HAADF scanning transmission electron micrograph of such a disordered network. The disorder, which is a product of self-organization during dealloying, is characterized by the complete absence of translational symmetry and an abundant variety of different curvatures that arise from local variation in edge length and connectivity (see also Figure 1c). To visualize the distribution of plasmonic modes of the network, we map the EELS signal, centered at 1.8 eV within a spectral window of 0.33 eV (Figure 4c). We observe large fluctuations in EELS intensity (Figure 4c) which is linked to the local density of optical states (LDOS).<sup>[43]</sup> Such fluctuations confirm both the highly inhomogeneous spatial distribution of the plasmonic eigenmodes and their ability to localize energy at nanometric scales in so-called “hot-spots”, that is, regions of high field intensities.<sup>[44]</sup>

To demonstrate the effect of disorder on the localization in the network, we probe three different hot-spots with a fixed area of  $10 \text{ nm}^2$  (Figure 4b) and compare the corresponding EELS spectra in Figure 4d. Remarkably, all three hot-spots localize polychromatic light very effectively while their spectra have quasi identical line-shape featuring the same broadband response  $\Delta\omega = 1.80 \pm 0.07 \text{ eV}$  centered at 1.8 eV. We can infer the formation of such a broadband plasmonic response to the disorder in the system, causing an equal distribution of the input energy between all plasmonic modes of the network.<sup>[42,45]</sup> Here, the localization length of these modes appears large enough, so they can extend over several “hot-spots”,<sup>[46]</sup> resulting in a delocalized “global” plasmonic response of the network. Reminiscent to connected wire-mesh metamaterials,<sup>[47]</sup> these global network modes (GNMs) rather rely on the connectivity of the network.<sup>[42,43]</sup>

To study the interaction of the network modes and LSP modes, we investigate the EELS probability in the vicinity of ellipsoidal NPs. The ellipsoidal NPs were specifically chosen for their large aspect ratio  $\zeta$ , defined as the ratio of the long semi-axes to short semi-axes. Compared to spherical NPs, these particles exhibit an increased local near-field enhancement, which in case of spatial mode overlap can result in an increased coupling between the nanoparticle and network mode.<sup>[34]</sup> Figure 5a,b II each show the EELS intensity of network modes in the vicinity of a single ellipsoidal Sn NP. The signal is strongly modulated and radially decreasing around the NP, suggesting that the mode spectrum is significantly modified and energy is exchanged.

To describe this mode coupling and its radial dependence in more detail, it is convenient to divide the area around the NP in thin nanometric shells. To only consider the high field regions of the dipolar mode of the Sn NPs (Figure 3a I), the shells are further divided into four sectors using the orientation (long axis)

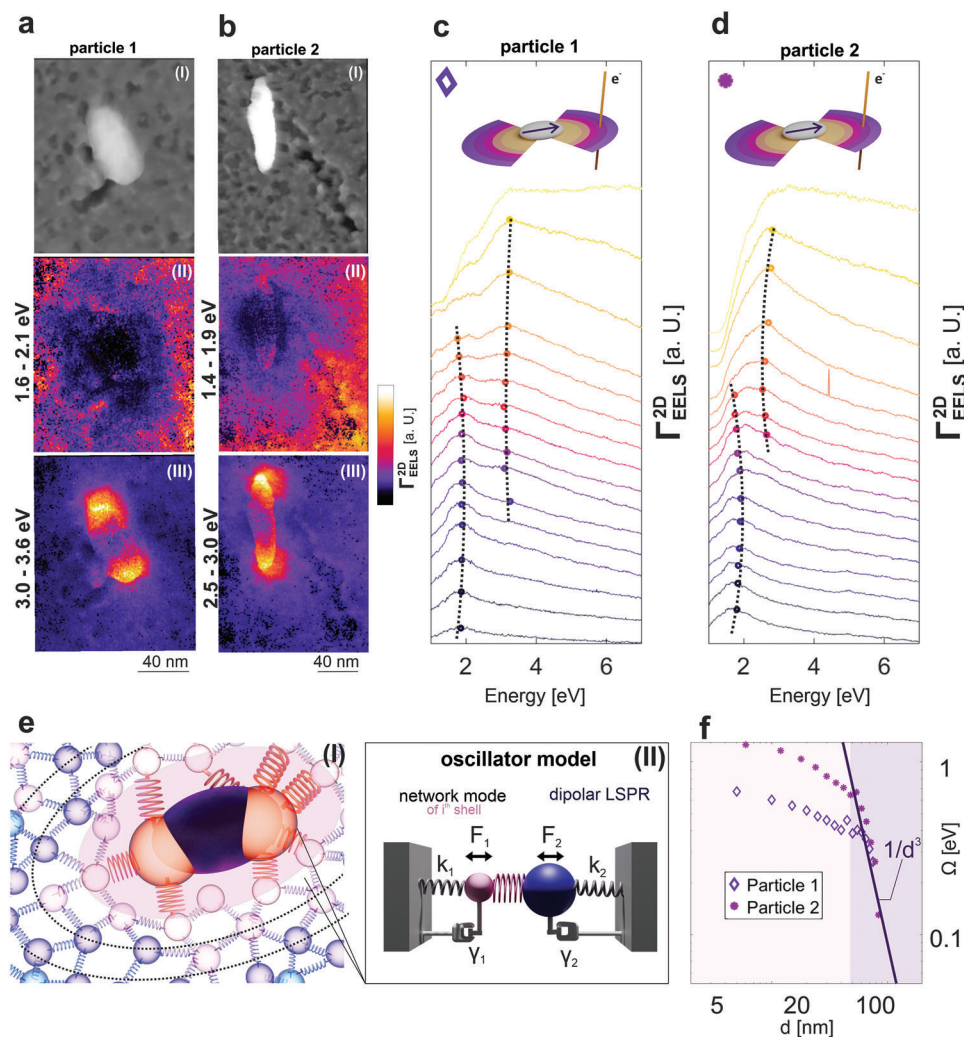


**Figure 5.** Mode Coupling a,b) (I) HAADF image of disordered two-phase metamaterials with color-coded maps of network mode (II) and dipolar mode (III). c,d) Waterfall plot of EEL spectra averaged in the shell sectors around nanoparticles 1 and 2, where the dipolar mode of the Sn NP is dominant. The color transition from yellow to orange to violet, corresponds to an increased in shell number around the NPs. Peak maximas (GNM and dipolar mode) from fitting the oscillator model to the experimental data are indicated by colored dots in the EEL spectra. The peak shift of both modes is indicated by a dotted black line. The figure inset shows schematically the division of the EELS maps into sector shells around the NP e) (I) Schematic illustration of the coupling between the GNM and the dipolar nanoparticle mode with the first shell around the NP shaded in pink. (II) Schematic illustration of the oscillator model, that is, two forced damped coupled harmonic oscillators. f) Calculated coupling constant  $\Omega$  for particle 1 (purple diamond,  $\zeta_{NP_1} = 2$ ) and particle 2 (pink star,  $\zeta_{NP_2} = 4$ ) as a function of the distance  $d$  to the Sn NP. The two different coupling regimes are shaded in purple, weak coupling with  $\Omega$  scaling with  $1/d^3$  and pink indicating strong coupling in close proximity to the nanoparticle.

of the NPs. A more detailed approach to the segmentation of the EELS maps is found in Supporting Information.

By calculating the average EELS spectrum in each shell, we retrieve the evolution of the EELS spectra at discrete distances around the nanoparticle (Figure 5c,d). Here, we limit ourselves to sectors in direction of the long axis of the Sn NPs, while the other direction is given in Supporting Information. In the waterfall plots in Figure 5c,d, we find that the spectra of the GNM ( $\approx 1.8$  eV) and the dipolar LSP ( $\approx 3$  eV) clearly shift when moving away from the NP center. The dashed trend line in Figure 5c,d suggests avoided crossing<sup>[48]</sup> of the GNM and the dipolar mode, a phenomena where two modes first approach and then repel each other. Avoided crossing is evocative of mode coupling.

To paint a fuller physical picture, we use a set of coupled damped harmonic oscillators to model the mode coupling.<sup>[49]</sup> To simplify, we disregard inter-shell interactions and only consider interaction of one effective network mode with the dipolar LSP mode within a single shell (Figure 5e I).

In the quasi-static limit, the two driven coupled oscillators (Figure 5e II) located at positions  $r_i$  and driven by the force  $F(r_i, t)$  are described by the effective Hamiltonian

$$H = \sum_{i=1}^N \frac{p_i^2}{2m_i} + \frac{1}{2} m_i \omega_i^2 Q_i^2 - \sum_{i \neq j} Q_i \Omega_{ij} Q_j - \sum_{i=1}^N F(r_i, t) Q_i, \quad (1)$$

where  $Q_i$  and  $P_i$  represent the displacement coordinate and conjugate momentum,  $m_i$  the effective mass, and  $\omega_i$  the resonance frequency of the  $i$ th dipolar mode. Furthermore,  $\Omega_{ij}$  is the coupling strength for pairwise near-field dipole-dipole interaction. A detailed discussion on the model solution and shell fitting can be found in Supporting Information. We find good agreement between the experimental data and our model, in terms of peak width and spectral position. The maxima of the modeled spectra are indicated by colored dots in Figure 5c,d and connected by a dashed trend line.

Moreover, the coupled oscillator model can be used to determine the coupling strength  $\Omega_{ij}$  between the global network mode and the dipolar LSP mode in each cell. The fitted coupling constant  $\Omega$  as a function of  $d$  is shown in Figure 5f for the two selected particles.

In case of two classically interacting dipoles, we expect  $\Omega$  to follow  $1/d^3$  in the near-field.<sup>[50]</sup> We observe this scaling for the outer shells, visible in Figure 5f, shaded in light purple. In this region  $\Omega < \omega_i$  the interaction lie in the weak coupling regime.

An important finding of our analysis is observed with  $d$  becoming smaller ( $d < 50\text{nm}$ ), where  $\Omega \approx \omega_i$  stops to follow  $1/d^3$  (Figure 5f, shaded in light pink) and is accompanied by significant peak broadening (Figure 5c,d). The observed increase in coupling strength  $\Omega$  can be associated with the difference in aspect ratio  $\zeta_{NP1} = 2$  and  $\zeta_{NP2} = 4$  of the two particles. This finding indicates a change in the coupling regime from weak to strong coupling in close proximity to the Sn NPs, as  $\Omega$  approaches  $\omega_i$ . We therefore find striking similarities between our system and the break down of dipol-dipol interaction in NP dimers with ultra small gaps.<sup>[50]</sup> The observed mode coupling outlines the possibility of energy exchange between the disordered network metamaterial and a second system over a large area. Realizing energy exchange, that is, mode coupling in novel materials based on self-assembly, offers pathways toward large scale energy materials for plasmon-enhanced catalysis.

### 3. Conclusion

In conclusion, we have experimentally demonstrated a general principle based on sequential self-assembly for fabricating large-area two-phase metamaterials with a transition from weak to strong coupling between the two different phases. By selecting two specific self-assembly reactions, namely phase separation and chemical dealloying, a two-phase metamaterial consisting of a disordered Cu network metamaterial and Sn nanoparticles has been manufactured. Engineering of the size and shape of the nanoparticles and the network<sup>[43]</sup> is readily achieved by altering the deposition parameters. Thereby, the self-organization during growth provides a versatile mechanism to modify the plasmonic response of the nanoparticle phase. As our approach relies on basic thermodynamic principles, it may apply to other ternary systems with a miscibility gap and also to systems with the tendency to form metastable intermetallics.

Electron energy loss spectroscopy allowed for fundamental insight in the modal properties of these two-phase metamaterials. We presented first experiments showing inhomogeneous localization of optical energy in “hot spots” of the network. The spectra of plasmonic eigenmodes measured in different “hot-spots” of the network are quasi identical, suggesting that the network

provides a means for energy equipartition. Previous experimental works<sup>[42,43]</sup> studying similar networks in the context of perfect absorbers, imply that a significant fraction of these plasmonic eigenmodes are accessible from the far field.

Beyond the localization of light in the network phase, we demonstrate that mode-coupling is achieved between the plasmonic modes of the network and the nanoparticles. In close proximity to the nanoparticle, the system transitions to the strong coupling regime which goes alongside with a breakdown of the classical dipole-dipole interaction. This presents a promising approach for designing a variety of coupled two-phase metamaterials which may include a dielectric phase or active phase, such as quantum dots, in addition to the plasmonic phase.

The possibility to design complex coupled systems solely by self-assembly and the ability to effectively localize polychromatic light at the nanoscale, offer unique opportunities to exploit these two-phase metamaterials as a platform for light harvesting and plasmon-enhanced chemistry.

### 4. Experimental Section

**Sample Fabrication:** The samples were created by a two step process. In a first step, Al-Cu-Sn thin films were co-sputtered onto commercial carbon supported gold TEM-grids. In a second step, the films were chemically dealloyed in a 1 M NaOH aqueous solution, to form a disordered open-porous nano-network. Detailed deposition parameters are reported in Supporting Information.

**EELS Measurements:** All EEL spectra were obtained by a monochromated FEI Titan 60-300 with an imaging filter (Gatan GIF Quantum) operated in scanning mode at 300 kV. The spectra were acquired with a dispersion of 0.25, respectively, 0.1 meV per pixel. Additionally, all spectra were treated with the HQ Dark Correction plugin.

**EELS Data Processing:** Postprocessing of the EELS data included the alignment of the spectra with respect to the position of the zero-loss peak (ZLP), normalization of the maximum intensity of the ZLPs in each pixel and removal of the ZLP by fitting of a premeasured ZLP using the Matlab Spectrum image analysis tool<sup>[37]</sup> and DigitalMicrograph (Gatan). Additionally, a script for DigitalMicrograph was developed to analyse the EEL spectra in relation to the distance from a selected particle.

**Simulations:** Complementary simulations were performed using the MNPBEM toolbox with the Sn nanoparticles modeled as an extruded ellipse.<sup>[37]</sup> The dielectric function of Sn was approximated by a Drude-Lorentz model  $\epsilon(\omega) \approx \epsilon_\infty - \frac{\omega_D^2}{\omega(\omega + i\gamma_D)} - \sum_{n=1}^{N_L} \frac{\epsilon_{Ln}\omega_{Ln}^2}{\omega(\omega + 2i\delta_{Ln})^2 - \omega_{Ln}^2}$  whereby  $\epsilon_\infty = 1.203$ ,  $\hbar\omega_D = 12.439$  (eV) and  $\hbar\gamma_D = 0.757$  (eV) taken from McMahon *et. al.*<sup>[38]</sup>

### Supporting Information

Supporting Information is available from the Wiley Online Library or from the author.

### Acknowledgements

The authors cordially thank the Graz Centre for Electron Microscopy for allowing access to their facilities. The authors acknowledge the technical support of FIRST as well as BRNC. The authors were also grateful to Nikolaus Porenta and Julian Gujer for their help and support. The authors thank Joan Sendra and Rebecca Gallivan for useful comments and careful reading of the manuscript. This project was funded in part by the European Union's Horizon 2020 research and innovation programme under grant agreement no. 823717 – ESTEEM3.

Open access funding provided by Eidgenössische Technische Hochschule Zurich.



## Author Contributions

J.W., H.G., and G.H. conceived the research plan. J.W. fabricated the samples. J.W. and G.H. collected EELS maps. J.W., H.G., and G.H. performed the data analysis. J.W. and H.G. wrote the manuscript and visualized the data. All authors reviewed and commented the manuscript.

## Conflict of Interest

The authors declare no conflict of interest.

## Data Availability Statement

The data that support the findings of this study are available from the corresponding author upon reasonable request.

## Keywords

chemical dealloying, disordered photonics, EELS, large-scale metamaterials, networks, plasmonics, self-assembly, strong coupling, two-phase systems

Received: March 8, 2023

Revised: May 26, 2023

Published online:

- [1] R. Long, Y. Li, L. Song, Y. Xiong, *Small* **2015**, *11*, 3873.
- [2] D. F. Swearer, B. B. Bourgeois, D. K. Angell, J. A. Dionne, *Acc. Chem. Res.* **2021**, *54*, 3632.
- [3] H. Hu, T. Weber, O. Bienek, A. Wester, L. Hüttenhofer, I. D. Sharp, S. A. Maier, A. Tittl, E. Cortés, *ACS Nano* **2022**, *16*, 13057.
- [4] S. Deng, B. Zhang, P. Choo, P. J. M. Smeets, T. W. Odom, *Nano Lett.* **2021**, *21*, 1523.
- [5] L. Yuan, M. Lou, B. D. Clark, M. Lou, L. Zhou, S. Tian, C. R. Jacobson, P. Nordlander, N. J. Halas, *ACS Nano* **2020**, *14*, 12054.
- [6] E. Cortés, W. Xie, J. Cambiasso, A. Jermyn, R. Sundaraman, P. Narang, S. Schlucker, S. Maier, *Nat. Commun.* **2017**, *8*, 14880.
- [7] K. Sytwu, M. Vadai, J. A. Dionne, *Adv. Phys.: X* **2019**, *4*, 1619480.
- [8] C. Zhang, H. Zhao, L. Zhou, A. E. Schlather, L. Dong, M. J. McClain, D. F. Swearer, P. Nordlander, N. J. Halas, *Nano Lett.* **2016**, *16*, 6677.
- [9] Y. Wang, W. Shuangshuang, S. Zhang, O. Scherman, J. Baumberg, T. Ding, H. Xu, *Nano Res.* **2018**, *11*, 6384.
- [10] T. Ding, J. Mertens, A. Lombardi, O. Scherman, J. Baumberg, *ACS Photonics* **2017**, *4*, 12615.
- [11] K. Friston, M. Levin, B. Sengupta, G. Pezzulo, *J. R. Soc., Interface* **2015**, *12*, 20141383.
- [12] G. M. Whitesides, B. Grzybowski, *Science* **2002**, *295*, 2418.
- [13] X. Shi, K. Ueno, T. Oshikiri, Q. Sun, K. Sasaki, H. Misawa, *Nat. Nanotechnol.* **2018**, *13*, 953.
- [14] D. Franklin, Z. He, P. M. Ortega, A. Safaei, P. Cencillo-Abad, S.-T. Wu, D. Chanda, *Proc. Natl. Acad. Sci. USA* **2020**, *117*, 13350.
- [15] L. Li, Y. Liang, X. Zong, Y. Liu, *Opt. Express* **2020**, *28*, 695.
- [16] Z. Fusco, M. Rahmani, T. Tran-Phu, C. Ricci, A. Kiy, P. Kluth, E. Della Gaspera, N. Motta, D. Neshev, A. Tricoli, *Adv. Mater.* **2020**, *32*, 2002471.
- [17] R. W. Style, T. Sai, N. Fanelli, M. Ijavi, K. Smith-Mannschott, Q. Xu, L. A. Wilen, E. R. Dufresne, *Phys. Rev. X* **2018**, *8*, 011028.
- [18] B. Derby, Y. Cui, J. Baldwin, R. Arróyave, M. J. Demkowicz, A. Misra, *Mater. Res. Lett.* **2019**, *7*, 1.
- [19] J. W. Cahn, J. E. Hilliard, *J. Chem. Phys.* **1958**, *28*, 258.
- [20] R. Murray, US Patent 1628190, **1927**.
- [21] H. Galinski, T. Ryll, L. Schlagenhauf, F. Rechberger, S. Ying, L. J. Gauckler, F. C. Mornaghini, Y. Ries, R. Spolenak, M. Döbeli, *Phys. Rev. Lett.* **2011**, *107*, 225503.
- [22] G. Kostorz, in *Metals And Alloys: Phase Separation and Defect Agglomeration*, Springer, Dordrecht, The Netherlands **1995**, pp. 255–266.
- [23] J. Weissmüller, R. C. Newman, H.-J. Jin, A. M. Hodge, J. W. Kysar, *MRS Bull.* **2009**, *34*, 577.
- [24] Y. Lu, C. Wang, Y. Gao, R. Shi, X. Liu, Y. Wang, *Phys. Rev. Lett.* **2012**, *109*, 086101.
- [25] K. Ankit, B. Derby, R. Raghavan, A. Misra, M. J. Demkowicz, *J. Appl. Phys.* **2019**, *126*, 075306.
- [26] H. Kotadia, A. Panneerselvam, O. Mokhtari, M. Green, S. Mannan, *J. Appl. Phys.* **2012**, *111*, 074902.
- [27] M. Kociak, O. Stéphan, *Chem. Soc. Rev.* **2014**, *43*, 3865.
- [28] A. Hörl, G. Haberfehlner, A. Trügler, F.-P. Schmidt, U. Hohenester, G. Kothleitner, *Nat. Commun.* **2017**, *8*, 37.
- [29] V. Flauraud, G. D. Bernasconi, J. Butet, D. T. L. Alexander, O. J. F. Martin, J. Brugger, *ACS Nano* **2017**, *11*, 3485.
- [30] T. Simon, X. Li, J. Martin, D. Khlopin, O. Stéphan, M. Kociak, D. Gérard, *Proc. Natl. Acad. Sci. USA* **2022**, *119*, e2116833119.
- [31] M. Achèche, C. Colliex, H. Kohl, A. Nourtier, P. Trebbia, *Ultramicroscopy* **1986**, *20*, 99.
- [32] C. C. Ahn, O. L. Krivanek, R. P. Burgner, M. M. Disko, P. R. Swann, *EELS atlas: a reference collection of electron energy loss spectra covering all stable elements*, Gatan, Inc., Warrendale, Pa **1983**.
- [33] J. Ngantcha, M. Gerland, Y. Kihn, A. Rivière, *Eur. Phys. J.: Appl. Phys.* **2005**, *29*, 83.
- [34] J. Zuloaga, E. Prodan, P. Nordlander, *ACS Nano* **2010**, *4*, 5269.
- [35] A. Lalis, G. Tessier, J. Plain, G. Baffou, *J. Phys. Chem. C* **2015**, *119*, 25518.
- [36] F.-P. Schmidt, H. Ditlbacher, U. Hohenester, A. Hohenau, F. Hofer, J. R. Krenn, *Nano Lett.* **2012**, *12*, 5780.
- [37] U. Hohenester, A. Trügler, *Comput. Phys. Commun.* **2012**, *183*, 370.
- [38] J. M. McMahon, G. C. Schatz, S. K. Gray, *Phys. Chem. Chem. Phys.* **2013**, *15*, 5415.
- [39] S. Raza, S. Kadkhodazadeh, T. Christensen, M. Di Vece, M. Wubs, N. A. Mortensen, N. Stenger, *Nat. Commun.* **2015**, *6*, 8788.
- [40] G. D. Bernasconi, J. Butet, V. Flauraud, D. Alexander, J. Brugger, O. J. F. Martin, *ACS Photonics* **2017**, *4*, 156.
- [41] G. T. Forcherio, D. DeJarnette, M. Benamara, D. K. Roper, *J. Phys. Chem. C* **2016**, *120*, 24950.
- [42] H. Galinski, A. Fratalocchi, M. Döbeli, F. Capasso, *Adv. Opt. Mater.* **2017**, *5*, 1600580.
- [43] J. Wohlwend, A. S. Sologubenko, M. Döbeli, H. Galinski, R. Spolenak, *Nano Lett.* **2022**, *22*, 853.
- [44] V. Krachmalnicoff, E. Castanié, Y. De Wilde, R. Carminati, *Phys. Rev. Lett.* **2010**, *105*, 183901.
- [45] P. Mao, C. Liu, F. Song, M. Han, S. Maier, S. Zhang, *Nat. Commun.* **2020**, *11*, 1538.
- [46] M. I. Stockman, L. N. Pandey, L. S. Muratov, T. F. George, *Phys. Rev. Lett.* **1994**, *72*, 2486.
- [47] W.-J. Chen, B. Hou, Z.-Q. Zhang, J. Pendry, C. Chan, *Nat. Commun.* **2018**, *9*, 2086.
- [48] J. Bellessa, C. Bonnard, J. C. Plenet, J. Mugnier, *Phys. Rev. Lett.* **2004**, *93*, 036404.
- [49] C. Wadell, T. J. Antosiewicz, C. Langhammer, *Nano Lett.* **2012**, *12*, 4784.
- [50] S. K. Ghosh, T. Pal, *Chem. Rev.* **2007**, *107*, 4797.